

## Probing of micromagnetic configuration in manganite channels by transport measurements

I. Pallecchi,<sup>1</sup> A. Gadaleta,<sup>2</sup> L. Pellegrino,<sup>1</sup> G. C. Gazzadi,<sup>3</sup> E. Bellingeri,<sup>1</sup> A. S. Siri,<sup>1,2</sup> and D. Marré<sup>1,2</sup>

<sup>1</sup>CNR-INFM LAMIA, Corso Perrone 24, 16152 Genova, Italy

<sup>2</sup>Dipartimento di Fisica, Università di Genova, Via Dodecaneso 33, 16146 Genova, Italy

<sup>3</sup>CNR-INFM-National Research Center on nanoStructures and bioSystems at Surfaces-S3, Via G. Campi 213/A, 41100 Modena, Italy

(Received 18 July 2007; revised manuscript received 26 September 2007; published 1 November 2007)

We explore the possibility of tracking magnetization orientation in artificial structures patterned in  $\text{La}_{0.7}\text{Sr}_{0.3}\text{MnO}_3$  epitaxial films by magnetotransport measurements, exploiting the anisotropic magnetoresistance effect. We perform resistance measurements as a function of temperature, magnetic field, and angle between the applied in-plane magnetic field and the channel or crystalline axes in micrometric channels of different widths. We analyze quantitatively our results and extract information about magnetization easy axes, crystalline anisotropy, domain wall resistance, anisotropic magnetoresistance, energy of magnetic domain pinning, and magnetic reversal mechanisms. For channel widths larger than a few micrometers, the magnetization direction at low field ( $\leq 200$  Oe) is determined by magnetocrystalline easy axes, whereas for channel widths of  $\sim 1$   $\mu\text{m}$  or smaller, the shape anisotropy forces the magnetization to align along the channel axis. This gives a precise indication on how artificial patterning can be used to force the magnetization direction in manganite based spintronic devices. Values of magnetocrystalline constant up to  $8000$   $\text{J}/\text{m}^3$  and anisotropic magnetoresistance values between  $0.1\%$  and  $0.6\%$  are found. Our data also indicate that, in the low field ( $\leq 200$  Oe) hysteretic regime, magnetization reversal occurs by thermal activated hopping of domain walls, with a characteristic hopping distance of  $4$ – $5$  nm.

DOI: [10.1103/PhysRevB.76.174401](https://doi.org/10.1103/PhysRevB.76.174401)

PACS number(s): 75.47.Lx, 75.30.Gw, 75.60.-d

### I. INTRODUCTION

Nanosized magnetic materials are attracting more and more attention worldwide, in view of electronics and spintronic device applications. In particular, in the field of oxide nanospintronics, manganites are among the most studied compounds. A noteworthy potential is related to the recent improvements in nanopatterning techniques, applied to manganites, such as electron beam lithography,<sup>1</sup> local anodization by atomic force microscopy (AFM),<sup>2</sup> and focused ion beam (FIB).<sup>3</sup> FIB at low doses can also be used to drive a local ferromagnetic to paramagnetic transition by controlled damaging of ferromagnetic films.<sup>4</sup> However, with the decrease in magnetic length scale in the submicron range, some classical theories no longer account for the micromagnetic behavior of the system. An experimental investigation of the micromagnetic configuration of a specific system is extremely useful to probe the competition between the various energetic terms, namely, the Zeeman energy, which aligns the magnetization to the external field, the anisotropy energy, which aligns the magnetization along certain preferential directions (the magnetocrystalline anisotropy to minimize the spin-orbit energy and the shape anisotropy to minimize the magnetostatic energy), the energy for the formation of domain walls, which results from the competition of the exchange and anisotropy terms against the magnetostatic term, and the pinning energy of domains associated with a coercive field. In this work, the systems under investigation are channels patterned in epitaxial manganite films; indeed, manganite oxides, with their spin polarized transport and Curie temperature close to room temperature are good candidates for spintronic applications.

Measurements of the electrical resistance of mesoscopic systems can provide useful information concerning proper-

ties other than those directly related to transport, namely, they can yield detailed information concerning the behavior of the magnetization. Moreover, in submicrometric systems, nontransport properties to probe the magnetic configuration are inherently difficult to measure because of the small volume of material involved. Magnetic imaging methods such as magnetic force microscopy, on the other hand, are not directly quantitative, not easy to carry out, and also often ambiguous to interpret. Ordinary transport measurements, such as anomalous Hall effect and longitudinal magnetoresistance, which can be anisotropic and/or hysteretic, are much more easy and sensitive in this case.

Anisotropic magnetoresistance (AMR) in transition metal ferromagnets is accounted for by spin-orbit interaction,<sup>5-7</sup> that yields different scattering rates between current parallel and perpendicular to  $\mathbf{M}$ , due to opening of interband scattering channels with mixing of unpolarized  $s$  and polarized  $d$  states. AMR is defined as the difference of resistance for magnetization parallel ( $R_{\parallel}$ ) and perpendicular ( $R_{\perp}$ ) to the current, normalized to the average resistance value. In ferromagnetic metals, typically  $R_{\parallel} > R_{\perp}$ , while in ferromagnetic semiconductors and also in manganites,  $R_{\parallel} < R_{\perp}$ .<sup>8-10</sup> As anisotropic magnetoresistance saturates at relatively low fields, it is particularly interesting in view of applications: anisotropic magnetoresistive memories have been fabricated,<sup>11-13</sup> spin current devices can be realized in materials with strong spin-orbit interaction;<sup>14-17</sup> moreover, through spin-orbit coupling, it is possible to manipulate spin currents via electric fields,<sup>15,18-22</sup> which is much more convenient than via magnetic fields when approaching nanometer spatial scales.

Spin-orbit induced anisotropic magnetoresistance in manganites, differently from ferromagnetic transition metals, is thought to be an intraband effect, namely, related to an energy splitting of the  $e_g$  majority states.<sup>23</sup> The magnitude of

AMR is an intrinsic property of manganites determined by chemical composition, structural deformation, and strain.<sup>24</sup> It has been found to be in the range 0.01%–5% (Refs. 5 and 23–26) and to be weakly temperature dependent, except for a peak near the Curie temperature (Refs. 23 and 25–28), which suggests that AMR and colossal magnetoresistance (CMR) are caused by the same scattering mechanisms in *d* bands.

A few measurements of magnetotransport as a function of the orientation of the external in-plane magnetic field in manganite thin films have been carried out in literature.<sup>29–32</sup> In particular, anisotropic magnetoresistance in manganites have been studied experimentally by some authors.<sup>5,7,33</sup> In Ref. 24, anisotropic magnetoresistance has been investigated in ultrathin manganite films by field effect experiments and it has been found to be independent of the carrier concentration; this is in contrast with chemical doping results, thus revealing the role of lattice distortions in determining the anisotropic magnetoresistance. In Ref. 34, anisotropic magnetoresistance measurements in ultrathin manganite films have been used to study the magnetization switching at low field and low temperature. Strain induced anisotropic magnetoresistance in manganite films with grain boundaries has been investigated as well.<sup>35,36</sup> The role of the substrate stress in determining the easy axis has been ascertained.<sup>37–39,33</sup>

Magnetotransport characteristics often display hysteretic behavior. Hysteretic resistance changes are associated with formation and/or movement of domain walls. The domain walls are some tens of nanometers thick and may be pinned by local defects or features of artificial patterns having roughly the same size. This opens the possibility of controlling the magnetic configuration by suitable nanolithographic patterns. Moreover, scattering by domain walls also contributes to magnetoresistance. In strongly correlated systems such as manganites, the general theory that relates the width of domain walls in ferromagnets to exchange and anisotropy constants does not necessarily hold. As long as insulating and metallic phases may be in close competition, phase separation may occur at domain walls due to the strong spin gradients therein.<sup>40–42</sup> Indeed, domain wall resistance in manganites has been measured, and it turns out to be 1–4 orders of magnitude larger than that expected in a double exchange picture and orders of magnitude larger than in cobalt.<sup>43–45</sup> It is not an easy task to extract the possible contribution of domain walls to magnetoresistance, proportional to the number of domain walls in a series resistance picture, from other magnetoresistive effects such as anisotropic magnetoresistance.<sup>46</sup> However, it has been estimated theoretically that the contribution to magnetoresistance (MR) of domain wall scattering should be much smaller than that of AMR in manganites.<sup>27</sup> On the other hand, a domain wall MR of 0.1% has been measured in compressively strained  $\text{La}_{0.7}\text{Sr}_{0.3}\text{MnO}_3$  thin films by comparing the magnetoresistivity of a current path across a random “maze” magnetic domain configuration with the magnetoresistivity of a current path across a stripe domain configuration.<sup>43</sup>

In this work, we plan to study how the micromagnetic configuration in artificially patterned manganite channels is determined by the competition among the different energy contributions, namely, the Zeeman energy, the magnetocrystalline anisotropy, the shape anisotropy, the pinning energy,

and the thermal energy. We use magnetotransport properties as a probe. In particular, we measure the channel resistance as a function of the angle between the applied in-plane magnetic field and the channel axis at different temperatures and magnetic fields or else the resistance versus magnetic field at different temperatures and angles. The resistance is modulated with the periodicity of the angle between the magnetization and the applied current due to the spin-orbit induced anisotropic magnetoresistance. If domain wall resistance effects are negligible, this allows us to extract the magnetization orientation at any given magnitude of the external magnetic field at any given angle between the magnetic field and the channel axis or crystalline axes, at any given temperature, and, if hysteresis is present, for any given magnetic and thermal history. In turn, the equilibrium orientation of magnetization allows us to reconstruct the energy terms and extract information on easy axes, magnetocrystalline and shape anisotropy constants, pinning, AMR, and magnetization switching mechanisms. Thereby, such study, on one hand, allows us to investigate fundamental and extrinsic properties relevant to magnetic response and, on the other hand, provides essential information for fabrication of any kind of manganite based device such as spin valves and ferromagnetic single electron transistors.

## II. EXPERIMENT

We deposit  $\text{La}_{0.7}\text{Sr}_{0.3}\text{MnO}_3$  thin films (thickness  $t \sim 20$  nm) by pulsed laser ablation on (001)  $\text{SrTiO}_3$  substrates at temperature of 815 °C and oxygen pressure of  $6 \times 10^{-2}$  Torr. The films exhibit metallic and ferromagnetic behavior below  $T_{\text{MI}} \sim 300$  K.

We pattern large (width  $\sim 15$   $\mu\text{m}$ , length  $\sim 200$   $\mu\text{m}$ ) channels by optical lithography and wet etching in HCl. We obtain narrower channels (width  $\sim 5$   $\mu\text{m}$ ) by AFM local anodization<sup>2</sup> and narrower ones (width  $\sim 1$ – $0.2$   $\mu\text{m}$ ) by FIB milling. The latter technique enables direct, maskless fabrication of submicron and nanometer size structures by sputtering removal of the top layer with a high resolution ( $<10$  nm) ion beam. A dual beam system (FEI DB235M), combining a  $\text{Ga}^+$  FIB and a scanning electron microscope (SEM), is employed, allowing *in situ* inspection of the fabricated constrictions. In Fig. 1(a), a SEM image of a FIB patterned channel is shown, together with a sketch of the four-probe transport measurement configuration in Fig. 1(b). In this picture, the definitions of the angles used in this paper are as follows:  $\vartheta$  is the angle between the in-plane applied magnetic field and the channel axis (direction of the current  $I$ ) and  $\varphi$  is the angle between the local in-plane magnetization and the channel axis.

We carry out transport measurements in a Quantum Design Physical Property Measurement System (PPMS) with rotator option at temperatures from 10 to 300 K, in magnetic fields up to 50 000 Oe, and varying the angle  $\vartheta$  between the in-plane applied magnetic field and the sample from  $0^\circ$  to  $220^\circ$ .

## III. RESULTS

In Fig. 2, we present resistance versus  $\vartheta$  measurements at low magnetic field (100 Oe) and different temperatures of

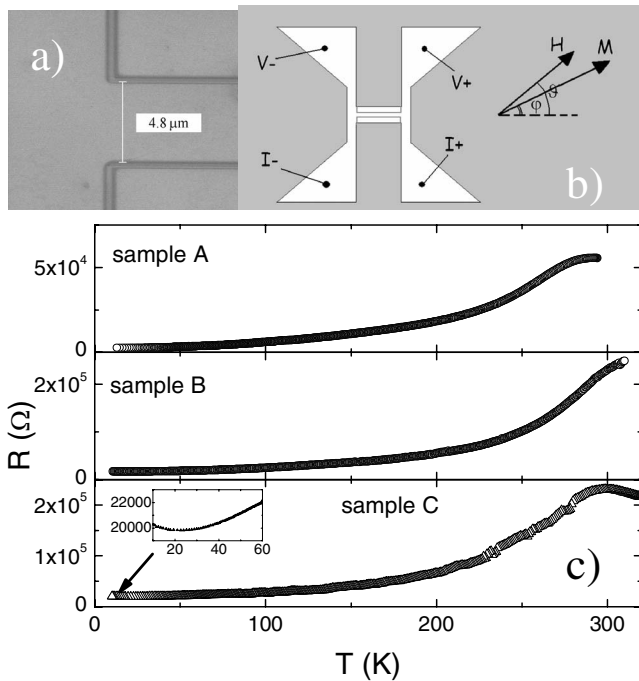


FIG. 1. (a) SEM image of a FIB patterned channel. (b) Sketch of the experimental setup for four-probe resistance measurements, with an in-plane applied magnetic field at angle  $\vartheta$  with the channel axis; the angle  $\phi$  between the magnetization and the current is also indicated. (c) Resistance versus temperature curves of the three samples whose behavior is shown in Figs. 2–4 (sample A, channel of  $13 \mu\text{m}$  width patterned by optical lithography), Figs. 5 and 6 (sample B, channel of  $4.5 \mu\text{m}$  width patterned by AFM local anodization), and Figs. 7 and 8 (sample C, channel of  $0.5 \mu\text{m}$  width patterned by FIB). In the case of sample C, the low temperature upturn is evidenced in the inset, whereas samples A and B exhibit metallic behavior down to 10 K.

50, 100, and 200 K of a  $13 \mu\text{m}$  wide channel parallel to the  $[100]$  crystalline direction (sample A). It can be seen that the curve shape resembles a triangular wave with minima around  $\vartheta=0^\circ$  ( $H\parallel I$ ) and maxima around  $\vartheta=\pm 90^\circ$  ( $H\perp I$ ). By closer inspection, it can be seen that at low temperature, the maxima (minima) are somewhat delayed with respect to  $\vartheta$

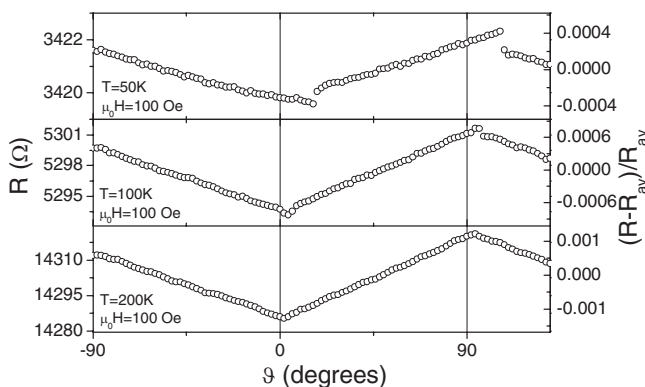


FIG. 2.  $R(\vartheta)$  curves at  $\mu_0 H = 100$  Oe and different temperatures measured on sample A.

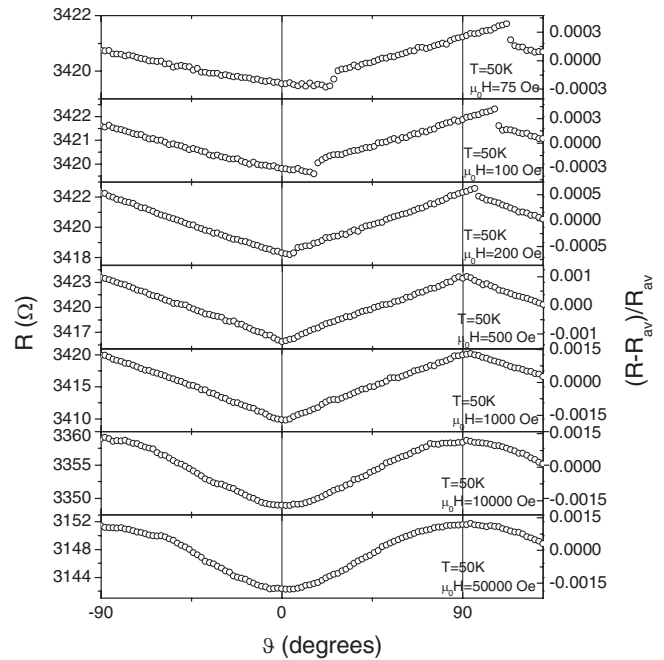


FIG. 3.  $R(\vartheta)$  curves at  $T = 50$  K and different in-plane magnetic fields measured on sample A.

$= \pm 90^\circ$  ( $0^\circ$ ), and the lower the temperature, the larger the delay. Moreover, at the lowest temperature (uppermost panel of Fig. 2), abrupt discontinuities are seen in correspondence to the changes of slope. At temperatures close to or larger than the Curie temperature  $\approx 300$  K, the curves are flat instead. In Fig. 3, resistance versus  $\vartheta$  curves at temperature of 50 K and different magnetic fields  $\mu_0 H$  from 75 to 50 000 Oe, measured on the same sample A, are shown. It can be seen that the curve shape undergoes a crossover from a triangular pattern with abrupt jumps for  $\mu_0 H \approx 75\text{--}200$  Oe to a triangular continuous pattern for intermediate  $\mu_0 H$  values of  $\approx 500\text{--}1000$  Oe and eventually to a sinusoidal pattern for fields larger than 1 T. In the right-hand axes, the relative resistance modulation around 0.1% is reported. As it will be shown in the following, in this case, the relative modulation is indicative of the AMR modulation only in the limit of sinusoidal shape, but not for the triangular shape whose amplitude is only a fraction of the AMR modulation.

In Fig. 4, the plot of resistance versus magnetic field intensity of sample A, measured at different angles  $\vartheta = 0^\circ, 45^\circ,$  and  $90^\circ$  and at temperature of 50 K, is presented. Before each  $R(H)$  cycle, the sample is demagnetized by oscillating the applied field down to zero with smaller and smaller cycles, so as to recover the same initial equilibrium configuration in all cases. It can be seen that the three curves are characterized by the same negative slope at large fields (around  $-0.0069 \Omega/\text{Oe}$ ), which is a signature of the tail of colossal magnetoresistance (CMR). Instead, at small fields ( $< 1000$  Oe), the curves are significantly different from one another, as better seen in the inset: the  $\vartheta = 0^\circ$  curve increases with magnetic field, the  $\vartheta = 90^\circ$  curve decreases faster than linearly, and the  $\vartheta = 45^\circ$  one is perfectly linear within experimental uncertainty.

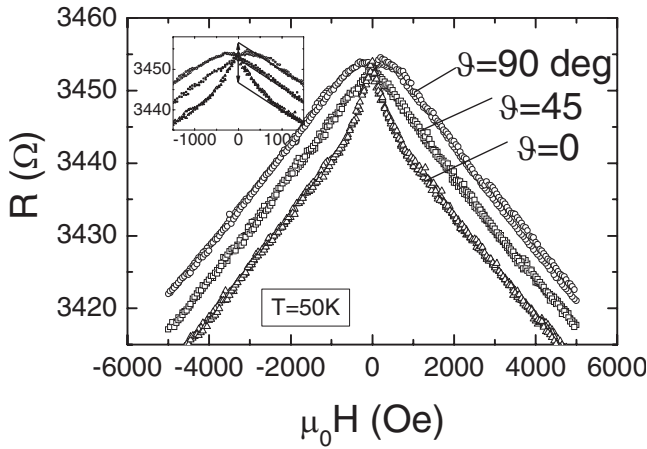


FIG. 4.  $R(H)$  curves at  $T=50$  K and different  $\vartheta$  measured on sample A. In the inset, a zoom on the low field region is shown in order to emphasize the departure from the high field linear slope.

We now describe the behavior of a narrower channel ( $4.5 \mu\text{m}$  width) parallel to the  $[100]$  crystalline direction, patterned by AFM lithography, which we call sample B. This sample has the largest metal-insulator transition temperature  $T_{MI}$ , indicating better structural quality and optimal oxygen stoichiometry, as seen in Fig. 1(c). In Fig. 5, we show resistance versus  $\vartheta$  measurements at  $\mu_0 H=200$  Oe and at different temperatures, which are very different with respect to those of Fig. 2. At low temperature, they have a square wave shape with steplike abrupt changes at  $\vartheta=\pm 45^\circ$ , which become increasingly rounded with increasing temperature and eventually become sinusoidal at 200 K. Similarly to sample A, at temperature close to  $T_{MI}$ , the behavior becomes flat. In Fig. 6, resistance curves at  $T=50$  K and at different applied fields are presented. Whereas at high field the sinusoidal shape resembles that of sample A, at low fields, the curves are squared; at fields as low as 75 Oe, the switching hardly occurs, and at 50 Oe, the rotating external field seems even to have no effect at all. It can be noticed that at low field and low temperature, the abrupt resistance steps are delayed with respect to  $\vartheta=\pm 45^\circ$ . In the right-hand axes, the relative resistance variation is, on the average, 0.1%–0.2%. In this

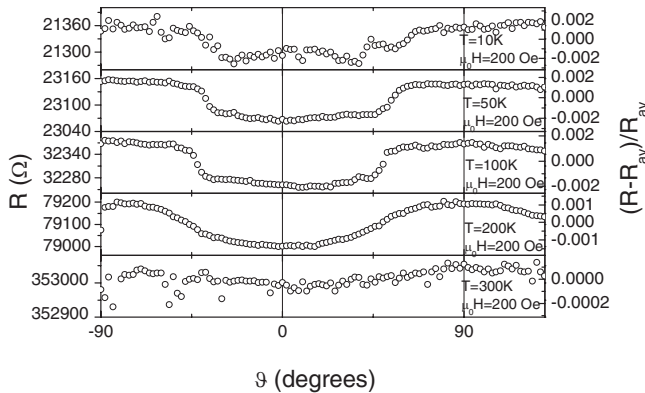


FIG. 5.  $R(\vartheta)$  curves at  $\mu_0 H=200$  Oe and different temperatures measured on sample B.

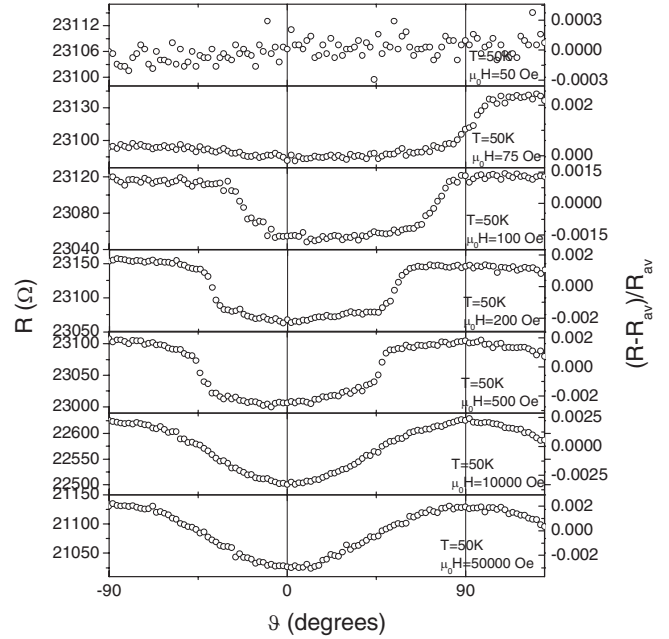


FIG. 6.  $R(\vartheta)$  curves at  $T=50$  K and different in-plane magnetic fields measured on sample B.

case, as it will be clarified in the next section, the relative modulation is indeed indicative of the AMR modulation.

In Fig. 7, we present an example of phenomenology of  $R(\vartheta)$  curves, which is qualitatively representative of all channels of width of  $1 \mu\text{m}$  or smaller, patterned by FIB. For this sample C, the high field behavior is sinusoidal as for the other samples described above, but at low field, a cusplike behavior with sharp maxima at  $\vartheta=\pm 90^\circ$  and broad minima at  $\vartheta=0^\circ$  is observed. At low field and low temperature, the cusps are delayed with respect to  $\vartheta=90^\circ$ .

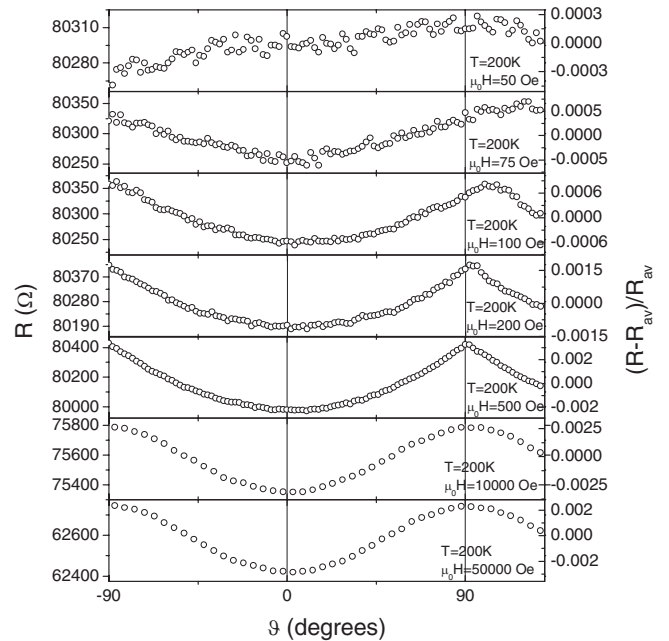


FIG. 7.  $R(\vartheta)$  curves at  $T=200$  K and different in-plane magnetic fields measured on sample C.

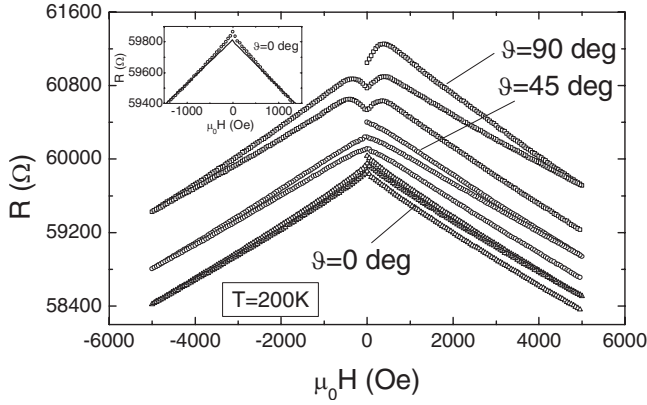


FIG. 8.  $R(H)$  curves at  $T=200$  K and different  $\vartheta$  measured on sample C. In the inset, a zoom on the low field region of the  $\vartheta=0^\circ$  curve is shown in order to emphasize the deviation from linearity.

Finally, the resistance versus field intensity at different angles and at  $T=200$  K is shown in Fig. 8. It is clearly seen that they do not close after a complete cycle. This apparent drift is likely a result of the magnetic history of the sample; in this sample with smaller  $T_{MI}$  and slight resistance upturn at low temperature [cf. Fig. 1(c) and the inset therein], the phase separation regime is likely extended well below the Curie temperature and the magnetic field cycles cause a spatial rearrangement and orientation of ferromagnetic regions along the current path, so that the measured resistance changes throughout the measurements. This effect is not related to the mechanisms discussed in this paper; thereby, we rather focus on the low field nonmonotonic behavior. In the  $\vartheta=90^\circ$  curve, there are maxima at nearly  $\pm 400$  Oe, while the  $\vartheta=45^\circ$  and  $\vartheta=0^\circ$  curves are monotonic, but the decrease of the former is lower than linear, while that of the latter is slightly larger than linear.

#### IV. DISCUSSION

In order to understand the different phenomenologies, we write the total free energy per unit volume of a uniformly magnetized system as a function of the angle  $\varphi$  between the magnetization and the current, neglecting as a first approximation the domain fragmentation:

$$\begin{aligned} \text{En}(\varphi) = & K_{\text{shape}} \sin^2 \varphi - \mu_0 M H \cos(\varphi - \vartheta) \\ & + K_{\text{cry}} \cos^2[2(\varphi - \alpha)]. \end{aligned} \quad (1)$$

Here,  $M$  is the saturation magnetization of  $\text{La}_{0.7}\text{Sr}_{0.3}\text{MnO}_3$  roughly constant with temperature well below the Curie temperature and equal to  $5.6 \times 10^5$  A/m.  $H$  is the applied field in A/m.  $K_{\text{cry}}$  is the magnetocrystalline anisotropy constant in  $\text{J/m}^3$ , whose value is found in literature to range between  $5 \cdot 10^3$   $\text{J/m}^3$  (Refs. 30, 37, and 47) and  $1.4 \cdot 10^4$   $\text{J/m}^3$  (Refs. 29, 32, 33, and 48), and is sensitively dependent on crystalline quality, strain, and defects (Refs. 28, 37, and 39).  $\alpha$  is an angle which defines the directions of the in-plane magnetization easy axes: in the notation of Eq. (1),  $\alpha=45^\circ$  indicates axes parallel and perpendicular to the channel axis, while

$\alpha=0^\circ$  indicates axes at  $\pm 45^\circ$  to the channel axis.  $K_{\text{shape}}$  is the shape anisotropy constant in  $\text{J/m}^3$  and, for a uniformly magnetized system, is related to the demagnetizing factors  $D_\perp$  and  $D_\parallel$  of the channel with perpendicular and parallel external fields, which can be calculated from geometrical parameters of the system:<sup>49</sup>

$$K_{\text{shape}} = \frac{\mu_0}{2} M^2 (D_\perp - D_\parallel). \quad (2)$$

We point out that the geometry of the channel determines the maximum value for  $K_{\text{shape}}$  through  $D_\perp$  and  $D_\parallel$ ; however,  $K_{\text{shape}}$  may be considerably lowered by fragmentation in magnetic domains which occurs to minimize the magneto-static energy of the system. In this case,  $K_{\text{shape}}$  is not anymore related to the channel width. In Eq. (2), the saturation magnetization  $M$  is a function of the temperature, but its weak variation can be neglected if the Curie temperature is not approached, which is our case for temperatures below 200 K.

For any given direction  $\vartheta$  and intensity  $H$  of the applied field, the equilibrium direction of the magnetization  $\varphi^*$  is found by minimization of the free energy of the system. Hence, the resistance of the channel can be calculated by the AMR formula

$$R = R_0 - \Delta R_{\text{AMR}} \cos^2 \varphi^*, \quad (3)$$

where  $R_0$  is the channel resistance when the magnetization is perpendicular to the current and  $\Delta R_{\text{AMR}}$  is the maximum variation of resistance due to the AMR mechanism, that is,  $\Delta R_{\text{AMR}} = R(M \parallel I) - R(M \perp I)$ . The relative change  $\Delta R_{\text{AMR}}/R$  is a property of  $\text{La}_{0.7}\text{Sr}_{0.3}\text{MnO}_3$  whose value is determined by the sample crystalline quality and stoichiometry, usually ranging between 0.01% and 0.4%,<sup>23–26</sup> up to a few percent;<sup>5</sup> it depends weakly on the magnetic field intensity<sup>24</sup> and also weakly on temperature, except that it has a sharp peak around the Curie temperature, possibly due to the enhanced spin-lattice interaction peaked at the Curie temperature.<sup>50</sup> It vanishes in the paramagnetic state.<sup>43–45</sup>

In order to distinguish the different regimes, in Fig. 9, we plot energy curves as a function of the magnetization direction  $\varphi$  from Eq. (1) for three different values of the direction of the applied field,  $\vartheta=0^\circ$ ,  $45^\circ$ , and  $90^\circ$  (first, second, and third columns, respectively). In the first row, the parameters are chosen in such a way that the crystalline anisotropy dominates over Zeeman and shape anisotropy terms and the two magnetization easy axes are parallel and perpendicular to the channel axis ( $K_{\text{cry}}=8000$   $\text{J/m}^3$ ,  $\mu_0 H=200$  Oe,  $K_{\text{shape}} < 300$   $\text{J/m}^3$ , and  $\alpha=45^\circ$ ). It can be seen that there are local energy minima along the easy axes  $\varphi=0^\circ$  and  $\varphi=\pm 90^\circ$ , and the lowest among them is determined by the direction of the applied field  $\vartheta$ . In the second row, the same parameters are kept, but the directions of the magnetization easy axes are fixed at  $\pm 45^\circ$  with respect to the channel axis ( $K_{\text{cry}}=8000$   $\text{J/m}^3$ ,  $\mu_0 H=200$  Oe,  $K_{\text{shape}} < 300$   $\text{J/m}^3$ , and  $\alpha=0$ ). The situation is very similar to the above one, but for the positions of the local minima at  $\varphi=\pm 45^\circ$ ,  $135^\circ$ ,  $225^\circ$ . In the third row, the case of dominating Zeeman energy is shown; the same anisotropy constants are assumed, but the field in-

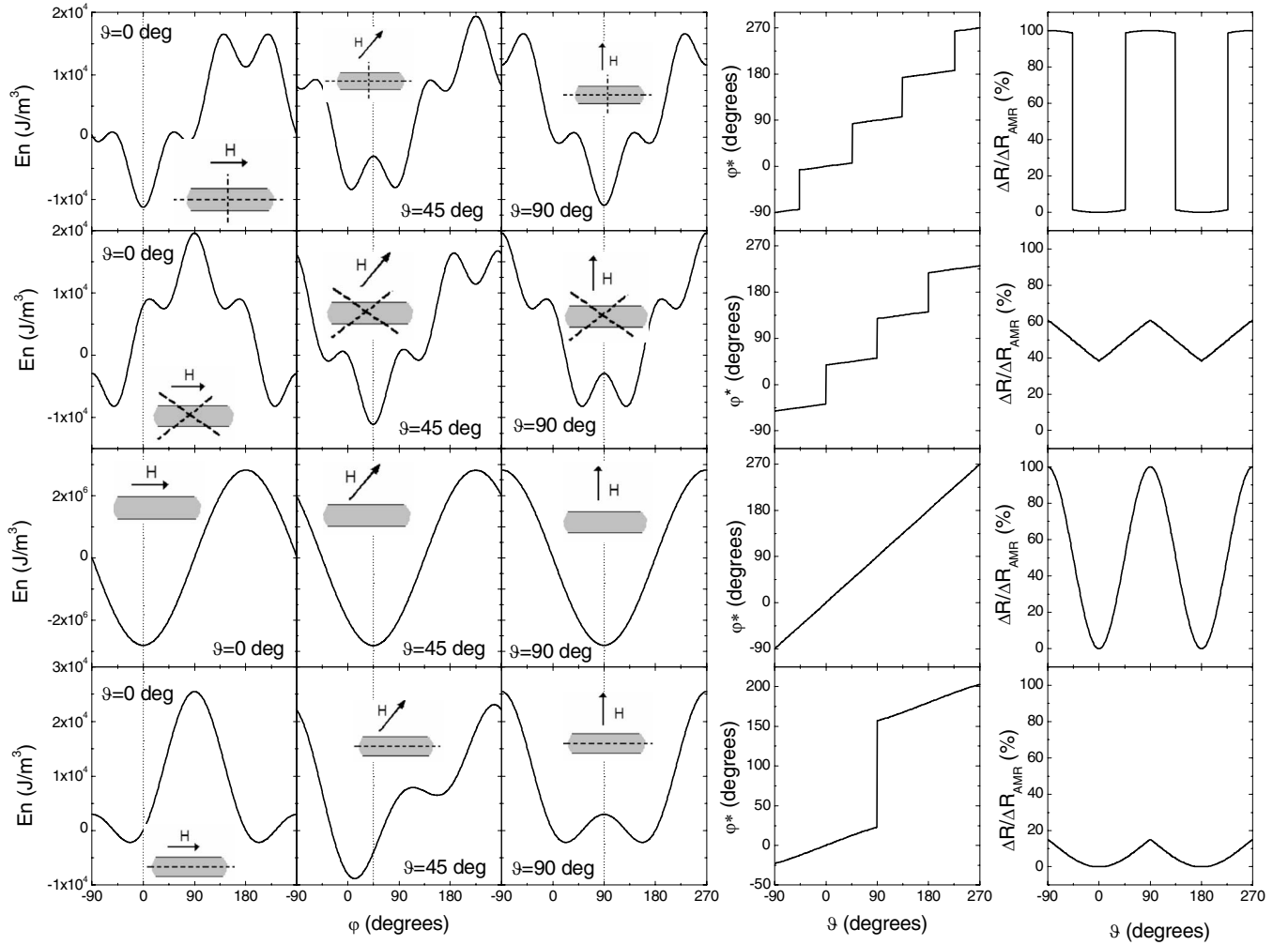


FIG. 9. First to third column: calculated free energy of a magnetic channel as a function of the magnetization direction  $\phi$  calculated by Eq. (1) for three directions  $\vartheta$  of the in-plane magnetic field. Fourth column: equilibrium magnetization direction calculated as absolute minimum of the free energy as a function of the direction  $\vartheta$  of the in-plane magnetic field. Fifth column: calculated resistance as a function of the direction  $\vartheta$  of the in-plane magnetic field according to Eq. (3). In the first row, the crystalline anisotropy dominates and the easy axes are parallel and perpendicular to the channel axis; in the second row, the crystalline anisotropy dominates and the easy axes are at  $\pm 45^\circ$  to the channel axis; in the third row, the Zeeman term dominates; and in the last row, the shape anisotropy dominates. The parameters are given in the text. In each panel, the channel and the orientation of  $H$  with respect to it are sketched; the dashed lines indicate the orientation of the magnetization favored by the anisotropy terms.

tensity is fixed at  $\mu_0 H = 50\,000$  Oe. In this case, the Zeeman minimum is so deep that it cancels out any effect of the anisotropies. Finally, in the last row, the shape anisotropy term dominates over the others ( $K_{\text{cry}} < 300$  J/m<sup>3</sup>,  $\mu_0 H = 200$  Oe, and  $K_{\text{shape}} = 1.4 \times 10^4$  J/m<sup>3</sup> corresponding to a width of a uniformly magnetized channel of  $0.4 \mu\text{m}$ ). The system has two local minima,  $\phi = 0^\circ$  and  $\phi = \pm 180^\circ$ , corresponding to magnetization parallel or antiparallel to the current, instead of the four minima characteristic of the crystalline anisotropy; again, the direction of the applied field selects the absolute minimum of the system. In the fourth column, the equilibrium direction of magnetization  $\phi^*$  is plotted versus the direction of the applied field  $\vartheta$ . When the crystalline anisotropy forces  $M$  to be either parallel or perpendicular to the channel axis (first column),  $\phi^*$  is a steplike function of  $\vartheta$ , and it increases very weakly around to favored directions, while it jumps abruptly across the forbidden

ranges. We point out that if a sizable shape anisotropy term was introduced, the perpendicular direction would be less favored than the parallel one and the steps would turn out unevenly spaced, with wider plateaus close to  $\phi^* = 0^\circ$  and  $\phi^* = 180^\circ$  and smaller ones close to  $\phi^* = 90^\circ$  and  $\phi^* = 270^\circ$ . When the crystalline anisotropy forces  $M$  to be at  $\pm 45^\circ$  or  $\pm 135^\circ$  to the channel axis (second row),  $\phi^*$  is again a steplike function of  $\vartheta$ , but with the steps shifted by  $45^\circ$ . When the Zeeman term dominates (third row), the system has only a stable minimum that shifts parallel to the direction of  $\vartheta$  and thereby  $\phi^*$  is always exactly aligned with  $\vartheta$ . Finally, if the shape anisotropy forces  $M$  to be either parallel or antiparallel to the current direction (fourth row),  $\phi^*$  is a steplike function of  $\vartheta$ , with weak linear increases around the favored direction  $\phi = 0^\circ/180^\circ$  and abrupt jumps in the forbidden intervals around the perpendicular direction. In the last column, the resistance calculated by Eq. (3) for the four situations is plot-

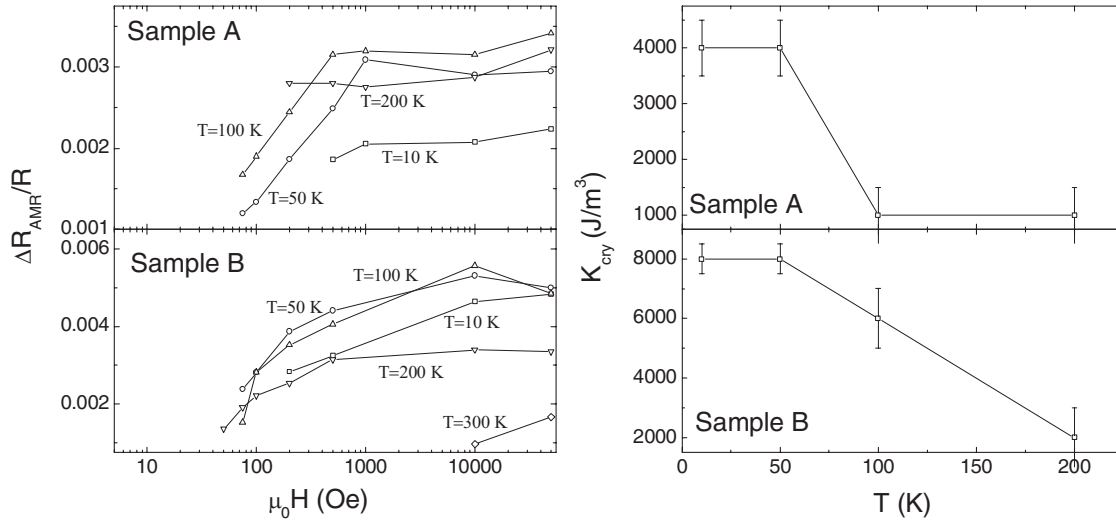


FIG. 10. Left-hand column: AMR versus applied in-plane magnetic field for samples A and B. Right-hand column: magnetocrystalline anisotropy constant  $K_{\text{cry}}$  extracted from the fitting procedure as a function of temperature.

ted. In the first case of crystalline anisotropy with easy axes parallel and perpendicular to the channel, the resistance is a square wave with maxima when the magnetization is perpendicular to the current and with minima when it is parallel. It can be noticed that the square wave amplitude is 100% of the AMR amplitude  $\Delta R_{\text{AMR}}$  of Eq. (3); therefore, in this condition, the experimental amplitude can be used to directly estimate the AMR. Moreover, the “duty cycle” of 50% guarantees that the parallel and perpendicular directions are equally favored, indicating negligible shape anisotropy. In the second row, with magnetization easy axes at  $\pm 45^\circ$  to the current,  $\varphi^*$  varies only within small ranges around  $\pm 45^\circ$  and  $\pm 135^\circ$ , which means that the  $\cos^2(\varphi^*)$  function varies around its flex points and the resistance curve is a cut-and-paste of these small almost linear segments around the flex points. In the third row, the Zeeman energy induces a linear variation of  $\varphi^*$  with  $\vartheta$  and thereby the resistance follows the  $\cos^2(\varphi^*)$  behavior exactly, with an amplitude equal to the AMR. Finally, the dominant shape anisotropy featured in the fourth row yields a resistance behavior with cusps, as the magnetization direction only assumes values around the parallel direction. The  $\varphi^*$  versus  $\vartheta$  curve results from cutting and joining intervals of the  $\cos^2(\varphi^*)$  function around the minima, with cusps appearing at the joints. In this case, as in the case of the second row, the amplitude of the angular dependence is a small fraction of the AMR resistance change.

With these premises, the experimental angular curves of Figs. 2, 3, and 5–7 can be understood pretty well and can be reproduced by suitable choice of the fitting parameters  $K_{\text{shape}}$ ,  $K_{\text{cry}}$ , and  $\alpha$  so as to gain information on the system.

Starting from the large channel A of Figs. 2–4, we find that the triangular shape of the resistance curve is obtained by assuming a dominant crystalline anisotropy term with easy axes at  $\pm 45^\circ$  to the channel axis, namely,  $[110]$  and  $[1-10]$  crystal directions. The  $K_{\text{cry}}$  constant can be determined in such a way to match the crossover from triangular to sinusoidal shape with increasing magnetic fields at the corresponding experimental values of  $H$ . For the curves of

Fig. 3, this criterion fixes  $K_{\text{cry}}$  in the range 3000–5000 J/m<sup>3</sup>. Alternatively, we can consider the  $R(H)$  curve of Fig. 4. At  $\vartheta=45^\circ$ , the curve is linear because  $H$  is parallel to one of the easy axes, and with increasing  $H$ , the magnetization does not change its direction; only the negative slope of CMR is measured. For  $\vartheta=0^\circ$ , the direction of the magnetization is initially along one of the easy axes at zero field, but it rotates and eventually aligns with  $H$  with increasing  $H$  intensity. Thereby, at  $\mu_0 H$  smaller than  $\sim 600$  Oe,  $\varphi^*$  decreases from  $45^\circ$  to  $0^\circ$  yielding a steep decrease in resistance, while at large fields, the AMR saturates and the resistance decreases with the characteristic slope of the CMR. For  $\vartheta=90^\circ$ , the magnetization rotates from  $\varphi^*=45^\circ$  to  $\varphi^*=90^\circ$  with increasing  $H$ , so that in the low field regime, the AMR increase dominates, while in the high field regime, the CMR decrease does. In this picture, by extrapolating the CMR slope to zero (see inset), we can evaluate the resistance difference  $R(M\parallel I) - R(M\perp I)$ , which is just the  $\Delta R_{\text{AMR}}$  term of Eq. (3), and we obtain  $\Delta R_{\text{AMR}}/R \approx 0.29\%$ . From the triangular  $R(\vartheta)$  curve at low field and at the same temperature (uppermost panel of Fig. 3), we obtain  $\Delta R_{\text{exp}}/R \approx 0.058\%$ . We are then able to estimate  $K_{\text{cry}}$  more precisely as the value which confines  $\varphi^*$  in the range around the easy axes in such a way that the triangular shape is a fraction  $f=0.058/0.29=20\%$  of  $\Delta R_{\text{AMR}}$ ; this criterion fixes  $K_{\text{cry}} \approx 4000$  J/m<sup>3</sup>, in agreement with the estimate based on the  $R(\vartheta)$  shape at different  $H$ . With this value, the magnetization direction  $\varphi^*$  spans a range of  $\pm 24^\circ$  around the easy axes. By the same arguments on similar measurements, we find 1000 J/m<sup>3</sup> at 100 and 200 K, besides the above mentioned 4000 J/m<sup>3</sup> at 50 and 10 K. These values are reported in the upper right-hand panel of Fig. 10. The decrease of the crystalline anisotropy constant with temperature, as well as its value, is consistent with results found by torque magnetometry.<sup>48</sup> We notice also that in these fits, the shape anisotropy constant must be assumed much smaller than  $K_{\text{cry}}$ , corresponding to an effective channel width larger than 20  $\mu\text{m}$  despite the channel is only 13  $\mu\text{m}$  wide. This indicates that the shape anisotropy is sig-

nificantly lowered by domain fragmentation, which occurs in order to minimize the magnetostatic energy of the system.

We now consider sample B of Figs. 5 and 6. Despite the smaller channel width, the squared shape is obtained again by assuming negligible  $K_{\text{shape}}$ , but, differently from sample A, by taking [100] and [010] magnetization easy axes that are parallel and perpendicular to the current. The difference between samples A and B lies mainly in the different orientations of the easy axes, rather than in their different widths. These different orientations appear as an inconsistency, but we point out that in literature, there is no univocal consensus about the magnetization easy axes in the (001) oriented manganite epitaxial thin films. We can say that 40% of literature papers indicate the [100] and [010] directions<sup>29,39</sup> and the other 60% indicate [110] and [1-10] (Refs. 30, 32, 48, and 51) instead. We believe that defects and oxygen vacancies yield a change in lattice parameters, causing a change in strain and magnetostriction, which changes the spatial symmetry of  $d$  orbitals and therefore of magnetization easy axes. Indeed, the crucial effect of strain on crystalline anisotropy has been well ascertained.<sup>37-39</sup> Even the anisotropy symmetry may be changed by strain: in (110) oriented epitaxial manganite films, uniaxial, rather than biaxial, anisotropy is observed.<sup>33,52</sup> Without making quantitative speculations on the strain, we simply notice that in Fig. 1(c), sample B has larger  $T_{\text{MI}}$  (above 310 K) than sample A (nearly 290 K), indicating probably a different content of oxygen. For sample B, we can estimate the value of  $K_{\text{cry}}$  which brings a crossover from square to sinusoidal shape in correspondence to the experimental values of  $\mu_0 H$  that are around 500 Oe at 10 and 50 K, around 200–500 Oe at 100 K, and below 75 Oe at 200 K. We find  $8000 \text{ J/m}^3$  at 10 and 50 K,  $6000 \text{ J/m}^3$  at 100 K, and  $2000 \text{ J/m}^3$  at 200 K. Again,  $K_{\text{cry}}$  decreases with decreasing temperature, even if the uncertainty of the fit is larger at larger temperature, due to thermal smearing that makes the squared behavior sinusoidal-like at smaller Zeeman energies. These results are reported in the lower right-hand side panel of Fig. 10. The slightly larger values of  $K_{\text{cry}}$  in sample B than in sample A confirm the better crystalline quality of the former.

Finally, we consider sample C of Figs. 7 and 8, patterned by FIB with a nominal width of  $4.8 \mu\text{m}$ . It is apparent from the channel resistance as compared to the resistance of larger channels patterned by optical lithography on the same film that the actual width of this sample is much smaller than the nominal value by a factor at least 5. Indeed, the high dose used for FIB patterning (of the order of  $10^{17}$  ions/cm<sup>2</sup>) has probably damaged the regions surrounding the grooves at the channel edges, due to the Gaussian profile of the ion beam, whose tails carry a non-negligible current intensity. A more careful study of this effect is underway; however, we found evidence that doses as low as  $2 \times 10^{13}$  ions/cm<sup>2</sup> are indeed effective in turning metallic ferromagnetic  $\text{La}_{0.7}\text{Sr}_{0.3}\text{MnO}_3$  into semiconducting and likely paramagnetic. An upper limit of the actual width of the ferromagnetic part of the channel can be extracted by the fitting value of the  $K_{\text{shape}}$  constant [ $K_{\text{shape}}$  fixes the maximum channel width in case of homogeneous magnetization by Eq. (2); if the magnetization is fragmented into domains, the same  $K_{\text{shape}}$  value may be found in narrower channels]. We are able to reproduce the crossover

from cusplike maxima to sinusoidal shape at  $\mu_0 H \approx 1000$  Oe as in Fig. 7 by assuming  $K_{\text{shape}} \approx 1.2 \times 10^4 \text{ J/m}^3$ , corresponding to a channel width of  $\sim 0.5 \mu\text{m}$  at most. Moreover, we have to assume that  $K_{\text{cry}}$  is smaller by at least 1 order of magnitude with respect to the other samples. We relate this low value to FIB induced damage; due to the sensitivity of  $K_{\text{cry}}$  to crystalline quality, this result is not surprising. In Fig. 1(c), it can be clearly seen that this sample has lower  $T_{\text{MI}}$  as well as resistance upturn at low temperature (see inset): These features are a signature of altered oxygen stoichiometry and disorder, possibly induced by strain and may well account for low crystalline anisotropy and extended temperature range of phase coexistence. However, we remark that FIB patterning has been successfully used to pattern manganite films down to nanometric size on shorter channel lengths ( $\sim 1 \mu\text{m}$ ).<sup>53</sup> With this choice of  $K_{\text{shape}} \approx 1.2 \times 10^4 \text{ J/m}^3$ , the amplitude of the angular variation of resistance  $\Delta R_{\text{exp}}/R$  at  $\mu_0 H = 100$  Oe is a fraction  $f \approx 4\%$  of  $\Delta R_{\text{AMR}}$  and the magnetization direction sweeps a range of angles of about  $\pm 13^\circ$  around  $\varphi^* = 0^\circ$  and  $\varphi^* = 180^\circ$ . In principle, we could as well obtain the value of  $\Delta R_{\text{AMR}}$  from the  $R(H)$  plots of Fig. 8 at 200 K, as done for sample A. However, this method leads to a value of  $K_{\text{shape}}$  of nearly one-half. Actually, it is clear that this sample is not magnetically stable at least at  $T = 200$  K due to phase separation. The magnetic configuration changes throughout the  $R(H)$  cycles due to spatial redistribution of metallic regions along the current path, and it is likely that even more severe changes occur from one kind of measurement to another. In a phase separation regime, the ferromagnetic domain size is undefined, and the  $K_{\text{shape}}$  value is not related to the channel width by Eq. (2). We think that the  $K_{\text{shape}}$  value that reproduces the whole set of  $R(\vartheta)$  curves with increasing  $H$  is more likely to approach the uniform magnetization limit of Eq. (2).

As a further check of the role of shape anisotropy term, we also measure channels whose axis was aligned along the [110] and [1-10] crystalline directions. The results are very similar to Fig. 7, indicating that the shape anisotropy term is determined by the artificial patterning and independent of the crystalline orientation. In some cases, the cusps are found to be slightly asymmetric; this is just expected in case of slight misalignment between channel axis and magnetization easy axes, if  $K_{\text{cry}}$  is not too much smaller than  $K_{\text{shape}}$ . The asymmetry may be even amplified if there is a sizable pinning of domain walls by defect of channel edge roughness.

Cusplike angular behavior characteristic of  $180^\circ$  symmetry has also been observed in much larger channels ( $\sim 65 \mu\text{m}$  width) in (110) epitaxial films<sup>33</sup> due to uniaxial crystalline anisotropy, which plays the role that belongs to shape anisotropy in our systems.

To summarize the AMR values found in our samples, we present in the left-hand panels of Fig. 10 the experimental data versus the applied field at different temperatures for samples A and B. All the values are around a few %. The data are directly measured in case of square and sinusoidal shapes; instead, for triangular and cusplike shapes, the experimental modulation is a fraction  $f$  of  $\Delta R_{\text{AMR}}$ , with  $f$  values which are obtained at each field  $H$  from the fitting procedure, so that the data are extrapolated by multiplying the

measured  $\Delta R_{\text{AMR}}$  by  $1/f$ . The AMR increases weakly with increasing  $H$ , similarly to what is found in Ref. 24, and also with increasing  $T$ , similarly to Refs. 23, 25, and 26; however, approaching the Curie temperature, it starts vanishing. This explains why the AMR curves at  $T=200$  K and  $T=300$  K tend to be smaller than at lower temperatures.

We now discuss the issue of the delayed switching of magnetization at low temperature and low field. This hysteretic effect is related to domain pinning by defects or by roughness at the edges of the artificially patterned channels. We compare the energy plots for  $\vartheta$  equal to the reversible switching angle and the delayed switching angle. The reversible switching angle is the one for which the absolute minimum of the energy versus  $\varphi$  plot changes from one well to the adjacent one as the direction of  $H$  rotates (for example, the switching angles are  $\vartheta=0^\circ$  and  $\vartheta=\pm 90^\circ$  for Figs. 2 and 3,  $\vartheta=\pm 45^\circ$  and  $\vartheta=\pm 135^\circ$  for Figs. 5 and 6, and  $\vartheta=\pm 90^\circ$  for Fig. 7). At large temperature, the system is actually able to jump to the absolute minimum, so that the magnetization rotates reversibly without hysteresis. Also at high field, the Zeeman minimum dominates and flattens the energy barriers between anisotropy minima. Instead, at low temperature, the magnetization may be frozen in a metastable state at the bottom of an energy well, until the energy barrier toward the absolute minimum is lowered enough by the rotation of  $H$ ; this occurs just when  $\vartheta$  reaches the delayed switching angle. Therefore, we calculate the difference in energy barriers at the reversible switching angle and at the delayed angle at any fixed temperature, and we compare such barrier difference with  $KT$  ( $K$  is the Boltzmann constant) divided by a volume, which we may call “switching volume”  $V_{\text{sw}}$ . Its meaning is a volume of magnetic coherence, as long as the magnetization switching cannot occur spin by spin, due to exchange coupling which would become too large if adjacent spins were too much misaligned from each other. If we further assume that along the 20 nm film thickness  $t$  domain fragmentation cannot occur, we can define a magnetic coherence length  $d_{\text{sw}}$  such that  $V_{\text{sw}}=d_{\text{sw}}^2 t$ . For all the samples, we measure delay angles which decrease with increasing  $T$ , yielding  $KT/V_{\text{sw}} \approx (4-6) \times 10^3$  J/m<sup>3</sup> and  $d_{\text{sw}} \approx 4-5$  nm. The magnetic coherence length  $d_{\text{sw}}$  is found to increase weakly in the above mentioned range with increasing  $T$  and  $H$ . We notice that  $V_{\text{sw}}$  is much smaller than the micrometric domain size and even smaller than the domain wall thickness of the order of some tens of nanometers.<sup>43,54</sup> Indeed,  $V_{\text{sw}}$  must not be confused with the domain size; instead, it can be rather thought of as the area spanned by a domain wall in its hopping during expansion or shrinkage of adjacent domains. In the case of sample B, the delay angle from  $\vartheta=-45^\circ$  is smaller than the delay angle from  $\vartheta=45^\circ$ , which is probably an effect of domain pinning. This may indicate that the morphology of channel edges caused by AFM patterning is more effective in pinning domain walls than those caused by FIB patterning and optical lithography. A rough estimate of the pinning energy can be obtained just by comparing the difference in the delay angles from  $\vartheta=-45^\circ$  and  $\vartheta=45^\circ$  and it turns out to be  $\sim 200$  J/m<sup>3</sup>.

It is mandatory to make some consideration about scattering by domain walls and its possible contribution in the resistance changes, which we have neglected up to now. It

could be argued that when the magnetization is aligned along an unfavorable direction, domain fragmentation is more likely to occur as in the case of stripe domains which form as a result of competing anisotropies.<sup>43,55,56</sup> If a large number of domain walls are encountered along the current path, a domain wall scattering term should be considered when analyzing  $R(\vartheta)$  curves, which we have so far interpreted only in terms of AMR of a uniformly magnetized system. Indeed, despite in standard transition metals such as Co domain wall scattering is negligible with respect to AMR [resistance-area product of  $7.8 \times 10^{-17}$   $\Omega$  m<sup>2</sup> (Ref. 57)], it has been suggested that in manganites, the large gradient of spin orientation at domain walls may trigger local phase transitions and thereby enhanced scattering.<sup>40-42</sup> Attempts to measure domain wall scattering resistance in manganites have been carried out.<sup>43,45</sup> and values of resistance-area product around  $10^{-13}-10^{-15}$   $\Omega$  m<sup>2</sup> have been found always larger than the values predicted by double exchange theory by orders of magnitude; however, these values have been measured either in compressively strained<sup>43</sup> or narrow bandwidth<sup>45</sup> manganites, where phase separation is strongly favored, differently from our  $\text{La}_{0.7}\text{Sr}_{0.3}\text{MnO}_3$  systems. To further support our approach, however, we put forward a few arguments. Usually, scattering by domain walls is thought to manifest itself as a low-field low-temperature magnetoresistance with a slope as a function of  $H$  steeper than the CMR slope. On the contrary, in our samples A and B, the measured  $R(H)$  are perfectly linear within experimental uncertainty if  $H$  is aligned along one of the magnetization easy axes ( $\vartheta=45^\circ$  curve in Fig. 4), ruling out domain scattering resistance contribution. Moreover, current-voltage characteristics of the channels at all fields and temperatures are fully Ohmic. Finally, we observe in the left-hand panels of Fig. 10 that the AMR tends to increase with increasing  $H$ , whereas a sizable domain scattering contribution would yield the opposite trend, as with increasing  $H$  the domains should expand and the number of domain walls should decrease. Only in FIB patterned samples a slight deviation from linearity at very low fields in the  $R(H)$  curves is observed (e.g., Fig. 8, curve at  $\vartheta=0^\circ$  and inset). This can be due to AMR if we assume thermally induced disorientation of magnetic domains around the equilibrium value  $\varphi=0^\circ$  at  $\mu_0 H=0$ , which may indeed occur a  $T=200$  K; alternatively, if we assume that all domains are in their equilibrium orientation  $\varphi=0^\circ$  at  $\mu_0 H=0$ , this deviation from linearity may be related to domain wall scattering. If the latter is the case, it is confirmed that domain wall scattering is appreciable only in samples whose domain walls are pinned at grain boundaries or regions with depressed ferromagnetism, which are possibly present in FIB patterned phase separated and strained channels. However, though appreciable, this deviation from linearity gives a contribution to resistance which is 1 order of magnitude smaller than the AMR contribution.

From the shape of the  $R(H)$  cycles, information about the switching mechanism can be gained. For example, it has been suggested that superlinear and/or sublinear behavior of  $R(H)$  curves with  $H$  parallel to the magnetization easy axis may indicate formation of transverse domains along the direction midway between two magnetization easy axes during

magnetization rotation;<sup>29,33</sup> it has also been suggested that abrupt hysteretic jumps indicate domain pinning and single domain behavior.<sup>29</sup> In our  $R(H)$  curves, none of these effect is seen, indicating that magnetization reversal occurs in a multidomain scenario by domain wall motion, with shrinking of domains along one of the easy axes and enlargement of other domains along the next easy axis as the magnetic field rotates.

## V. CONCLUSIONS

In this work, we provide precise indications about the ranges of temperature, magnetic field, and artificial patterning size, which are relevant for fabrication of manganite based spintronic devices, and we also demonstrate that transport measurements are a suitable tool to track the magnetization direction in  $\text{La}_{0.7}\text{Sr}_{0.3}\text{MnO}_3$  channels. In particular, we find that for channel widths larger than a few micrometers, the magnetization direction at low field is determined by magnetocrystalline easy axes, whereas for channel widths of  $\sim 1 \mu\text{m}$  or smaller, the shape anisotropy forces the magnetization to align along the channel axis, indicating that this is the average domain size at low temperature. Hysteretic ef-

fects due to anisotropy and/or pinning are observed at temperature of 50 K or smaller and fields of up to 200 Oe. At larger temperatures, the magnetization rotates reversibly with the applied field, but its direction is determined by anisotropy rather than by the external field as long as  $\mu_0 H$  is smaller than 200 Oe.

We find values of magnetocrystalline constant up to  $8000 \text{ J/m}^3$  in the samples of good crystalline quality and AMR values around a few %, which slightly increase with  $H$  and  $T$  well below  $T_{\text{MI}}$ . We also find that the magnetocrystalline easy axes can be either [100] and [010] directions or [110] and [1-10] directions, depending on the crystalline quality and strain. Finally, our experimental data indicate that, in the low field ( $\leq 200$  Oe) hysteretic regime, the magnetization reversal mode is by thermally activated domain walls hopping, with a characteristic area swept in each hopping event of  $\sim 20 \text{ nm}^2$ .

## ACKNOWLEDGMENTS

The authors acknowledge support from EU under the project NANOXIDE, Contract No. 033191.

- 
- <sup>1</sup>T. Arnal, R. Soulimane, A. Aassime, M. Bibes, Ph. Lecoeur, A. M. Haghiri-Gosnet, B. Mercey, A. V. Khvalkovskii, A. K. Zvezdin, and K. A. Zvezdin, *Microelectron. Eng.* **78-79**, 201 (2005).  
<sup>2</sup>L. Pellegrino, E. Bellingeri, A. S. Siri, and D. Marré, *Appl. Phys. Lett.* **87**, 064102 (2005).  
<sup>3</sup>I. Pallecchi, L. Pellegrino, A. Caviglia, E. Bellingeri, G. Canu, G. C. Gazzadi, A. S. Siri, and D. Marré, *Phys. Rev. B* **74**, 014434 (2006).  
<sup>4</sup>A. Ruotolo, S. Wiebel, J. P. Jamet, N. Vernier, D. Pullini, J. Gierak, and J. Ferré, *Nanotechnology* **17**, 3308 (2006).  
<sup>5</sup>J. N. Eckstein, I. Bozovic, J. O'Donnell, M. Onellion, and M. S. Rzchowski, *Appl. Phys. Lett.* **69**, 1312 (1996).  
<sup>6</sup>E. D. Dahlberg, K. Riggs, and G. A. Prinz, *J. Appl. Phys.* **63**, 4270 (1988).  
<sup>7</sup>G. J. Snyder, M. R. Beasley, T. H. Geballe, R. Hiskes, and S. DiCarolis, *Appl. Phys. Lett.* **69**, 4254 (1996).  
<sup>8</sup>Y. Pu, E. Johnston-Halperin, D. D. Awschalom, and J. Shi, *Phys. Rev. Lett.* **97**, 036601 (2006).  
<sup>9</sup>T. Jungwirth, J. Sinova, K. Y. Wang, K. W. Edmonds, R. P. Campion, B. L. Gallagher, and C. T. Foxon, *Appl. Phys. Lett.* **83**, 320 (2003).  
<sup>10</sup>B. Zhao, X. Yan, and A. B. Pakhomov, *J. Appl. Phys.* **81**, 5527 (1997).  
<sup>11</sup>A. V. Pohm, J. Daughton, C. Comstock, Yoo Hah, and Hur Jae, *IEEE Trans. Magn.* **23**, 2575 (1987).  
<sup>12</sup>A. V. Pohm, J. S. T. Huang, J. M. Daughton, D. R. Krahn, and V. Mehra, *IEEE Trans. Magn.* **24**, 3117 (1988).  
<sup>13</sup>K. Pappert, S. Hümpfner, C. Gould, J. Wenisch, K. Brunner, G. Schmidt, and L. W. Molenkamp, *Nat. Phys.* **3**, 573 (2007).  
<sup>14</sup>S. Murakami, N. Nagaosa, and S. C. Zhang, *Science* **301**, 1348 (2003).  
<sup>15</sup>J. Sinova, D. Culcer, Q. Niu, N. A. Sinitsyn, T. Jungwirth, and A. H. MacDonald, *Phys. Rev. Lett.* **92**, 126603 (2004).  
<sup>16</sup>Y. K. Kato, R. C. Myers, A. C. Gossard, and D. D. Awschalom, *Science* **306**, 1910 (2004).  
<sup>17</sup>J. Wunderlich, B. Kaestner, J. Sinova, and T. Jungwirth, *Phys. Rev. Lett.* **94**, 047204 (2005).  
<sup>18</sup>S. Murakami, N. Nagaosa, and S. C. Zhang, *Phys. Rev. B* **69**, 235206 (2004).  
<sup>19</sup>J. Schliemann and D. Loss, *Phys. Rev. B* **69**, 165315 (2004).  
<sup>20</sup>E. I. Rashba, *Phys. Rev. B* **68**, 241315(R) (2003).  
<sup>21</sup>A. A. Burkov, A. S. Núñez, and A. H. MacDonald, *Phys. Rev. B* **70**, 155308 (2004).  
<sup>22</sup>B. A. Bernevig and S. C. Zhang, *Phys. Rev. B* **72**, 115204 (2005).  
<sup>23</sup>M. Ziese and S. P. Sena, *J. Phys.: Condens. Matter* **10**, 2727 (1998).  
<sup>24</sup>X. Hong, J.-B. Yau, J. D. Hoffman, C. H. Ahn, Y. Bason, and L. Klein, *Phys. Rev. B* **74**, 174406 (2006).  
<sup>25</sup>M. Bibes, V. Laukhin, S. Valencia, B. Martínez, J. Fontcuberta, O. Yu Gorbenko, A. R. Kaul, and J. L. Martínez, *J. Phys.: Condens. Matter* **17**, 2733 (2005).  
<sup>26</sup>M. Ziese, *Phys. Rev. B* **62**, 1044 (2000).  
<sup>27</sup>M. Ziese, *Rep. Prog. Phys.* **65**, 143 (2002).  
<sup>28</sup>M. Egilmez, R. Patterson, K. H. Chow, and J. Jung, *Appl. Phys. Lett.* **90**, 232506 (2007).  
<sup>29</sup>J. O'Donnell, M. Onellion, M. S. Rzchowski, J. N. Eckstein, and I. Bozovic, *Phys. Rev. B* **55**, 5873 (1997).  
<sup>30</sup>Moon Ho Jo, N. D. Mathur, J. E. Evetts, and M. G. Blamire, *Appl. Phys. Lett.* **77**, 3803 (2000).  
<sup>31</sup>Moon-Ho Jo, N. D. Mathur, and M. G. Blamire, *Appl. Phys. Lett.* **80**, 2722 (2002).  
<sup>32</sup>R. Gunnarsson and M. Hanson, *Phys. Rev. B* **73**, 014435 (2006).  
<sup>33</sup>I. C. Infante, D. Hrabovský, V. Laukhin, F. Sanchez, and J. Fontcuberta, *J. Appl. Phys.* **99**, 08C503 (2006).

- <sup>34</sup>Y. Bason, L. Klein, J.-B. Yau, X. Hong, J. Hoffman, and C. H. Ahn, *J. Appl. Phys.* **99**, 08R701 (2006).
- <sup>35</sup>H. S. Wang and Q. Li, *Appl. Phys. Lett.* **73**, 2360 (1998).
- <sup>36</sup>C. Srinithiwarawong and M. Ziese, *Appl. Phys. Lett.* **73**, 1140 (1998).
- <sup>37</sup>Y. Suzuki, H. Y. Hwang, S.-W. Cheong, T. Siegrist, R. B. van Dover, A. Asamitsu, and Y. Tokura, *J. Appl. Phys.* **83**, 7064 (1998).
- <sup>38</sup>F. Tsui, M. C. Smoak, T. K. Nath, and C. B. Eom, *Appl. Phys. Lett.* **76**, 2421 (2000).
- <sup>39</sup>Y. Suzuki, H. Y. Hwang, S.-W. Cheong, and R. B. van Dover, *Appl. Phys. Lett.* **71**, 140 (1997).
- <sup>40</sup>N. D. Mathur and P. B. Littlewood, *Solid State Commun.* **119**, 271 (2001).
- <sup>41</sup>D. I. Golosov, *Phys. Rev. B* **67**, 064404 (2003).
- <sup>42</sup>M. S. Rzchowski and R. Joynt, *Europhys. Lett.* **67**, 287 (2004).
- <sup>43</sup>Y. Wu, Y. Suzuki, U. Rüdiger, J. Yu, A. D. Kent, T. K. Nath, and C. B. Eom, *Appl. Phys. Lett.* **75**, 2295 (1999).
- <sup>44</sup>T. Arnal, A. V. Khvalkovskii, M. Bibes, B. Mercey, Ph. Lecoeur, and A. M. Haghiri-Gosnet, *Phys. Rev. B* **75**, 220409(R) (2007).
- <sup>45</sup>N. D. Mathur, P. B. Littlewood, N. K. Todd, S. P. Isaac, B. S. Teo, D. J. Kang, E. J. Tarte, Z. H. Barber, J. E. Evetts, and M. G. Blamire, *J. Appl. Phys.* **86**, 6287 (1999).
- <sup>46</sup>M. Viret, D. Vignoles, D. Cole, J. M. D. Coey, W. Allen, D. S. Daniel, and J. F. Gregg, *Phys. Rev. B* **53**, 8464 (1996).
- <sup>47</sup>R. Akiyama, H. Tanaka, T. Matsumoto, and T. Kawai, *Appl. Phys. Lett.* **79**, 4378 (2001).
- <sup>48</sup>K. Steenbeck and R. Hiergeist, *Appl. Phys. Lett.* **75**, 1778 (1999).
- <sup>49</sup>A. Aharon, *J. Appl. Phys.* **83**, 3432 (1998).
- <sup>50</sup>A. I. Lobad, R. D. Averitt, C. Kwon, and A. J. Taylor, *Appl. Phys. Lett.* **77**, 4025 (2000).
- <sup>51</sup>P. Lecoeur, P. L. Trouilloud, G. Xiao, A. Gupta, G. Q. Gong, and X. W. Li, *J. Appl. Phys.* **82**, 3934 (1997).
- <sup>52</sup>Y. Suzuki, H. Y. Hwang, S. W. Cheong, and R. B. van Dover, *Appl. Phys. Lett.* **71**, 140 (1997).
- <sup>53</sup>O. Céspedes, S. M. Watts, J. M. D. Coey, K. Dorr, and M. Ziese, *Appl. Phys. Lett.* **87**, 083102 (2005).
- <sup>54</sup>S. J. Lloyd, N. D. Mathur, J. C. Loudon, and P. A. Midgley, *Phys. Rev. B* **64**, 172407 (2001).
- <sup>55</sup>J. Dho, Y. N. Kim, Y. S. Hwang, J. C. Kim, and N. H. Hur, *Appl. Phys. Lett.* **82**, 1434 (2003).
- <sup>56</sup>Z.-H. Wang, G. Cristiani, H.-U. Habermeier, Z.-R. Zhang, and B.-S. Han, *J. Appl. Phys.* **94**, 5417 (2003).
- <sup>57</sup>J. F. Gregg, W. Allen, K. Ounadjela, M. Viret, M. Hehn, S. M. Thompson, and J. M. D. Coey, *Phys. Rev. Lett.* **77**, 1580 (1996).